Nanoscale Advances

ROYAL SOCIETY OF CHEMISTRY

PAPER

View Article Online
View Journal | View Issue

Cite this: *Nanoscale Adv.*, 2025, **7**, 4490

Mo–P bond-induced MoS_2 fast electron transfer improves the lithium storage performance of MoS_2–MoP heterojunction†

Shasha Wang,[ab] Jiaqi Guo,[a] Jiaqi Huo,[a] Lu Wen,[a] Jingyao Tang,[a] Bo Cao[a] and Yan Cheng*[a]

Mo-based hybrids, including molybdenum oxide, molybdenum sulfide, and molybdenum carbide, have been extensively investigated as anode materials for lithium-ion batteries (LIBs) due to their high theoretical electrochemical capacities compared to conventional carbon materials. However, molybdenum phosphide, which shows great promise as an anode material for LIBs, has been scarcely investigated to date. In this paper, two-dimensional (2D) mesoporous ultrasmall MoS_2–MoP heterostructured nanosheets/graphene hybrids (meso-MoS_2–MoP/G) were synthesized using a "nanocasting" method followed by a phosphidation treatment. The as-prepared 2D meso-MoS_2–MoP/G hybrid featured unique mesoporous structures with MoS_2–MoP heterojunctions vertically growing on the graphene nanosheet. Benefiting from its characteristic nanosheet morphology, abundant mesopores, high electrical conductivity, and the unique MoS_2–MoP heterostructure, the 2D meso-MoS_2–MoP/G hybrid demonstrated exceptional lithium storage performance as an anode material for LIBs in terms of specific capacity, cycling stability, and long cycle life. The specific capacity of 2D meso-MoS_2–MoP/G hybrid remained above 910.3 mA h g^{-1} at a current density of 100 mA g^{-1} after 50 cycles. Even at a high current density of 1 A g^{-1}, the 2D meso-MoS_2–MoP/G hybrid still delivered a remarkable discharge capacity of 863.9 mA h g^{-1} with good cycling stability. This study provides an efficient approach to construct heterostructured nanosheets on 2D materials for high-performance LIBs.

Received 10th February 2025
Accepted 2nd May 2025

DOI: 10.1039/d5na00135h

rsc.li/nanoscale-advances

1. Introduction

Owing to the extensive combustion of fossil fuels, the greenhouse effect has become more severe, and environmental pollution has emerged as a critical issue in modern society.[1,2] Nanomaterials have been studied for use in clean and sustainable energy devices, such as batteries, solar cells, and capacitors.[3,4] LIBs offer numerous advantages, such as high energy density, lightweight design, desirable cycle life, and environmental friendliness; thus, they are regarded as one of the most promising energy storage systems.[5,6] Generally speaking, ideal electrode materials for LIBs should exhibit high electrical conductivity and specific surface area while being cost-effective and demonstrating long-term electrochemical stability.[7] Typically, carbon-based materials—particularly graphite—are the most widely used commercial anode materials in LIBs; however, they suffer from a relatively low theoretical capacity of 372 mA h g^{-1}, which significantly limits their application.[8–10] To further enhance the performance of LIBs, traditional graphite should be replaced by advanced materials with higher capacity. Tremendous research has been devoted to discovering or designing anode materials with high specific capacity for LIBs and which typically exhibit better lithium storage properties and higher energy densities than the existing systems.[11–14] As alternative electrode materials, transition metal oxides, nitrides, and sulfides have been widely reported.[15] Nevertheless, anode materials with high theoretical capacity often suffer from poor cycle stability due to drastic volume changes and severe particle aggregation during repeated cycling. These issues lead to the pulverization and exfoliation of anode materials from the current collector, resulting in poor cycling ability and rapid capacity decline.[5,16]

Recently, Mo-based materials have received intensive attention in the field of energy transformation and storage,[17,18] including oxygen reduction reactions (ORRs), hydrogen production (HER), and LIBs,[19] among others. More importantly, MoS_2 exhibits a high lithium storage capacity due to the weak van der Waals interactions between its (002) planes, which facilitate easy intercalation of Li^+ ions without causing significant volume expansion.[16,20,21] Various MoS_2-based

[a]*Inner Mongolia Engineering Center for Regional Resource Utilization and Eco-Environmental Protection, College of Chemistry and Environment Science, Inner Mongolia Normal University, Hohhot 010022, China. E-mail: ycheng@imnu.edu.cn*
[b]*Institute of Environmental and Health, Inner Mongolia Normal University, Hohhot, 010022, China*

† Electronic supplementary information (ESI) available. See DOI: https://doi.org/10.1039/d5na00135h

nanomaterials, such as MoS_2 nanosheets,[22,23] MoO_2/MoS_2/carbon,[24] MoSSe,[25] and MoS_2/C composites,[26,27] have been widely researched as anode materials for LIBs. Moreover, phosphorus (P), characterized by low electronegativity, serves as a promising alternative anion that can combine with transition metals (Mo, Co, Ni, Fe) to form effective electrode materials and enhance the electrochemical performance of LIBs. Yan *et al.*[28] reported a straightforward method involving simple mixing and annealing treatment to synthesize a composite of MoP@PC (molybdenum phosphide and porous carbon). Thanks to its advantageous microstructure and composition, the MoP@PC structure retains its nanodot morphology without any agglomeration, even after multiple charging–discharging cycles. Wang *et al.*[29] proposed a facile strategy to synthesize MoP/CNTs microspheres using a spray drying method followed by a phosphating process. The carbon nanotubes (CNTs) are embedded throughout the MoP/CNTs microspheres, which not only promotes the electrical conductivity of the composite but also alleviate volume changes during cycling. Shen *et al.*[30] proposed a meso-MoO_2/MoP-NBs composite, composed of uniform nanoparticles, obtained through a one-step phosphorization process. Benefiting from the synergistic effects, the meso-MoO_2/MoP-NBs exhibit remarkable cycling performance (515 mA h g^{-1} after 1000 cycles at 1 A g^{-1}) and excellent rate capability (291 mA h g^{-1} at 8 A g^{-1}). Wang *et al.*[31] reported a modification strategy involving the coating of heterostructured MoP–MoS_2 and porous carbon nanofibers onto the surface of a Celgard separator. The combination of heterostructured MoP–MoS_2 with carbon nanofibers effectively suppresses the shuttle effect of lithium polysulfides (LiPS), thereby enhancing the kinetics of catalytic reactions within the battery. Leveraging these advantages, the assembled Li–S battery featuring a MoP-50/PCNFs separator demonstrates an impressive specific capacity of 1090.02 mA h g^{-1}, along with a high discharge capacity of 884.67 mA h g^{-1} even after 300 cycles at 1C. These findings can provide insights into the behavior of electron/ion regulation in heterostructures and offer a potential route for developing high-performance lithium-ion storage materials. Thus, it can be predicted that endowing nanostructures, combined with graphene, and fabricating MoS_2–MoP heterojunctions can not only maximize the contact surface area between the MoS_2 electrode and electrolyte, shortening the diffusion paths for electrons and lithium ions, but also facilitate charge redistribution at the interface.

Based on the above investigation, we proposed a novel strategy to fabricate a two-dimensional (2D) mesoporous ultrasmall MoS_2–MoP heterostructured nanosheets/graphene hybrid (meso-MoS_2–MoP/G) as an anode material for LIBs. The as-prepared 2D meso-MoS_2–MoP/G hybrid possessed a unique mesoporous structure, with heterostructured MoS_2–MoP nanosheets vertically growing on the graphene nanosheet. This unique configuration offered significant advantages over traditional electrode materials: First, the 2D layered graphene, as a flexible conductive carrier, greatly enhanced the conductivity of the material. Second, the mesoporous heterostructured MoS_2–MoP nanosheets facilitated a shorter transfer distance for Li^+ ions and electrons, thereby enhancing the ion diffusion rate and optimizing the charge and discharge processes associated with volume effects. Third, the vertically oriented MoS_2–MoP nanosheets provided exceptional structural advantages that promoted effective multi-directional electron transfer pathways. Finally, the existence of the Mo–P bond enables strong coupling between MoS_2 and MoP, inducing rapid electron transfer in MoS_2 and enhancing its electrochemical performance. Due to its unique structure and composition, the 2D meso-MoS_2–MoP/G hybrid exhibited outstanding lithium storage performance as an anode material for lithium-ion batteries, demonstrating excellent specific capacity, cycling stability, and prolonged cycle life.

2. Results and discussion

2D meso-MoS_2–MoP/G was prepared *via* a "nanocasting" method followed by a calcination process. TEOS served as the silicon source in the template, and P123 acted as the structure-directing agent. During the calcination process, sodium hypophosphite was used as the phosphate source. Sodium hypophosphite, along with Mo and S precursors, was placed in different temperature zones of the tube furnace, as shown in Fig. 1a. The temperature of the left zone was maintained at 350 °C to ensure the decomposition of sodium hypophosphite and the production of PH_3 gas, which partially converted MoS_2, located in the high-temperature zone of the tube furnace, into MoP.

The XRD patterns of the obtained 2D meso-MoS_2–MoP/G hybrids calcined at 700 °C, 750 °C, and 800 °C are shown in Fig. 1b. The diffraction peaks at 26°, 37°, and 53.4° were attributed to the MoO_2 phase (JCPDS#86-0315). However, two weak peaks at 33° and 43°, corresponding to MoS_2 (JCPDS#37-1492) and MoP (JCPDS#24-0771), respectively appeared, indicating that the electrode material obtained at 700 °C was primarily the MoO_2 phase, accompanied by a small amount of MoS_2 phase. When the phosphidation temperature increased to 750 °C, the diffraction peaks assigned to MoO_2 disappeared, while the diffraction peaks at 14° and 33°, attributed to the MoS_2 phase, gradually increased. Meanwhile, the peak at 43°, identified as the MoP phase, was also observed. These results indicated that the electrode material obtained at 750 °C was MoS_2-dominant, with a small amount of MoP. When the temperature was further raised to 800 °C, the intensities of the diffraction peaks of MoP increased, while the peaks of the MoS_2 phase became weaker, indicating that a large amount of MoS_2 had been converted into MoP. The sample synthesized at 800 °C was a mixed phase of MoS_2 and MoP. The relatively broad diffraction peaks suggested that the confined effect of the mesopores in the KIT-6 template limited the growth of MoS_2 and MoP nanocrystals.

The samples obtained at different phosphidation temperatures were further investigated by SEM and TEM, and the results are shown in Fig. 2. Fig. 2a–c display the SEM images of the samples prepared at 700 °C, 750 °C and 800 °C, respectively. Clearly, a two-dimensional lamellar structure and corrugated graphene was observed in the SEM images, with the thickness of the lamellae approximately 40–50 nm. As the temperature

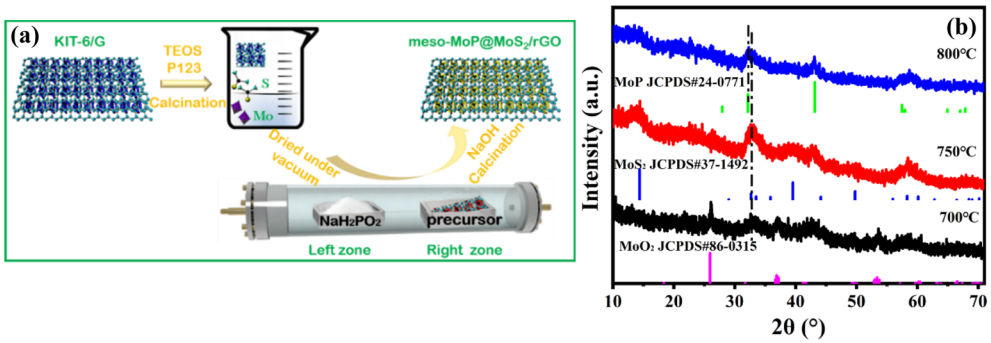

Fig. 1 (a) Schematic of the synthesis of meso-MoS_2–MoP/G hybrid. (b) XRD patterns of meso-MoS_2–MoP/G (700 °C), meso-MoS_2–MoP/G (750 °C), and meso-MoS_2–MoP/G (800 °C).

increased, the sample surface gradually became rougher due to the generation of more MoP nanocrystals at high calcination temperatures, which was consistent with the XRD results. Fig. 2d and e show the TEM images of meso-MoS_2–MoP/G obtained at 800 °C, where the lamellar structure with ultrasmall nanosheets (marked by red dotted circles) perpendicularly growing on the surface of the graphene sheet can be clearly observed.[32] This phenomenon was also confirmed by HRTEM. The lattice spacings in Fig. 2f were 0.70 nm and 0.27 nm, corresponding to the MoS_2 (002) crystal plane and MoP (100) crystal plane, respectively, suggesting the formation of a heterostructured MoS_2–MoP nanosheet.[33–35] From the SEM and TEM images, it could be seen that the addition of sulfur to the precursors was beneficial for obtaining a well-dispersed lamellar structure. Compared with MoP-based materials obtained using other precursors, the MoP obtained using MoS_2 as the precursor possessed an ultrasmall size and was well-dispersed on the surface of the lamellar MoS_2 structure. This structure increased the number of electron transport paths and facilitate the diffusion of lithium ions and electrons. The elemental mapping images revealed the uniform distribution of S, Mo, C, and P (Fig. 2g).

The pore structure and specific surface area of meso-MoS_2–MoP/G (700 °C), meso-MoS_2–MoP/G (750 °C), and meso-MoS_2–MoP/G (800 °C) were measured by nitrogen adsorption–desorption tests (Fig. 3). As shown in Fig. 3a, the nitrogen adsorption–desorption isotherms of the samples obtained at different phosphidation temperatures exhibited a type IV

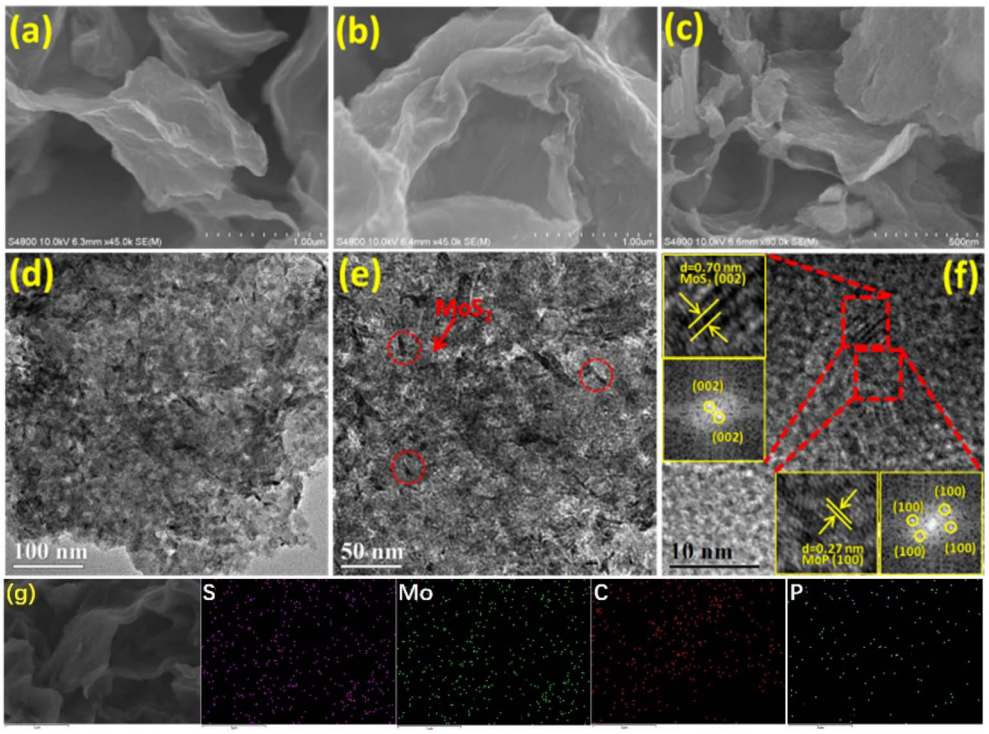

Fig. 2 (a–c) SEM images of meso-MoS_2–MoP/G (700 °C), meso-MoS_2–MoP/G (750 °C), and meso-MoS_2–MoP/G (800 °C), respectively; (d–f) TEM images of meso-MoS_2–MoP/G (800 °C), (g) elemental mapping of meso-MoS_2–MoP/G (800 °C).

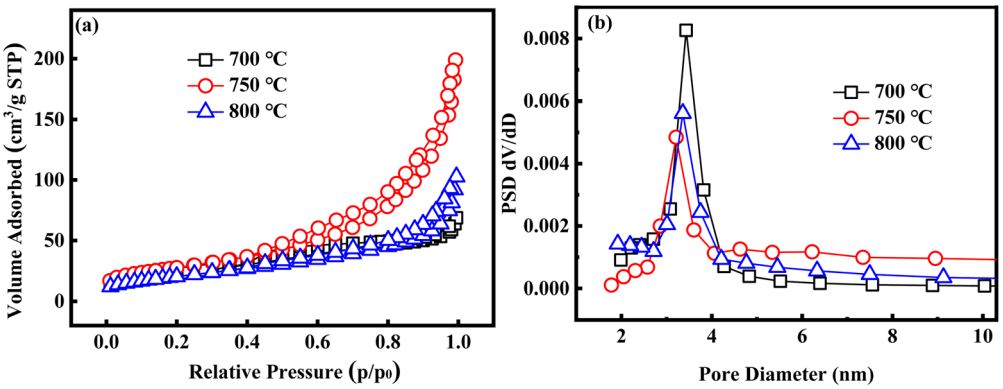

Fig. 3 (a) N_2 adsorption/desorption isotherms and (b) pore size distribution of meso-MoS_2–MoP/G (700 °C), meso-MoS_2–MoP/G (750 °C) and meso-MoS_2–MoP/G (800 °C).

isotherm with an H1 hysteresis loop at P/P_0 of 0.4–1.0, which was characteristic of the adsorption curve of typical ordered mesoporous materials. The specific surface areas of the electrode materials obtained at 700 °C, 750 °C, and 800 °C were 74.5 $m^2\ g^{-1}$, 99.0 $m^2\ g^{-1}$, and 80.9 $m^2\ g^{-1}$, respectively. The rich mesoporous characteristics of meso-MoS_2–MoP/G (750 °C) were possibly due to the reduction reaction between Mo^{6+} and H_2S during calcination, while the higher calcination temperature may cause the sintering of nanoparticles or structural collapse, leading to a reduction in porosity and surface area. The highest surface area of 2D meso-MoS_2–MoP/G (750 °C) suggested that it could provide more lithium-active sites during the electrochemical reaction process. In addition, the pore structure of meso-MoS_2–MoP/G (750 °C) was measured using the Barrett–Joyner–Halenda method. The pore volume of meso-MoS_2–MoP/G (750 °C) was 0.23 $cm^3\ g^{-1}$, with a pore size of 3.2 nm, which was the highest among the three electrode materials (Fig. 3b and Table S1†). Due to the large specific surface area and pore

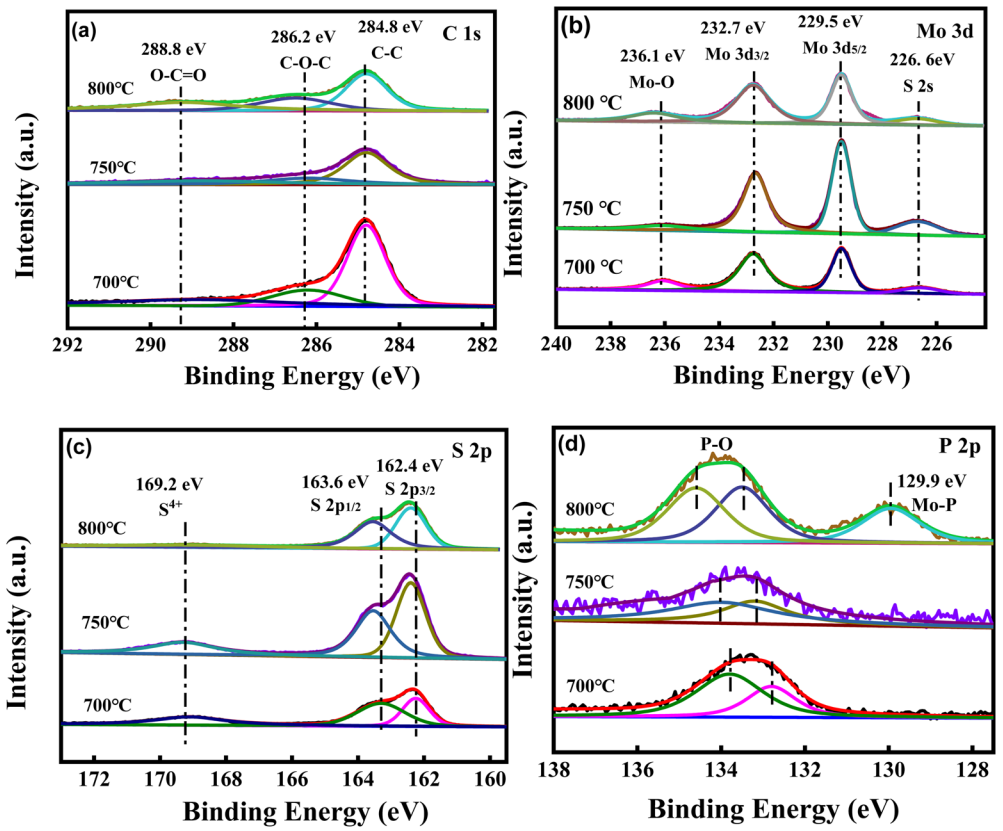

Fig. 4 XPS spectra of (a) C 1s, (b) Mo 3d, (c) S 2p, and (d) P 2p for meso-MoS_2–MoP/G (700 °C), meso-MoS_2–MoP/G (750 °C), and meso-MoS_2–MoP/G (800 °C).

volume, the obtained electrode material could effectively alleviate the volume change during the electrochemical reaction, provide more active sites, and enhance cycle performance.

XPS was used to investigate the surface electronic state and composition of the meso-MoS_2–MoP/G hybrids (Fig. 4). The overall XPS spectra showed the presence of Mo, S, P, and C. The C 1s spectrum was fitted with three components. The main peak (284.8 eV) was attributed to graphitic C–C, while the other two peaks at 286.2 and 288.8 eV were assigned to C–O and O–C=O, respectively (Fig. 4a).[31] For the XPS spectrum of Mo 3d for meso-MoS_2–MoP/G hybrids, two peaks at 232.7 (Mo^{4+} $3d_{3/2}$) and 229.5 eV (Mo^{4+} $3d_{5/2}$) were observed. The weak double peaks, corresponding to MoO_3, were observed at 236.1 eV, which resulted from slight oxidation on the surface of meso-MoS_2–MoP/G in air. The S $2p_{1/2}$ and $2p_{3/2}$ peaks, located at 163.6 and 162.4 eV, were attributed to S^{2-} species in MoS_2, while the high-energy component at 169.2 eV was assigned to S^{4+} species in sulfate groups (SO_3^{2-}) (Fig. 4b and c). Furthermore, a shift of the S 2p peaks toward higher binding energy occurred after phosphidation. The difference in work function was found to drive the redistribution of interface charges. This indicated a higher chemical state due to electron transfer between P and S.[36] This phenomenon confirmed that P was successfully doped into the MoS_2 matrix (Fig. 4c). The XPS spectra of P 2p are shown in Fig. 4d. After phosphidation at 700 °C, two broad peaks occurred at about 134 eV (133.9 and 133.1 eV), corresponding to the P–O of PO_4^{3-}.[36] When the phosphidation temperature was 750 °C, the peaks showed a slight shift, but no new peaks appeared. As the phosphidation temperature increased to 800 °C, the Mo–P peak became clearly visible. These results indicated that the MoP content in the meso-MoS_2–MoP/G hybrid gradually increased with temperature, which was consistent with the XRD results.[37] Additionally, the major P species located at 129.9 eV could be assigned to $P^{\delta-}$ bonded to

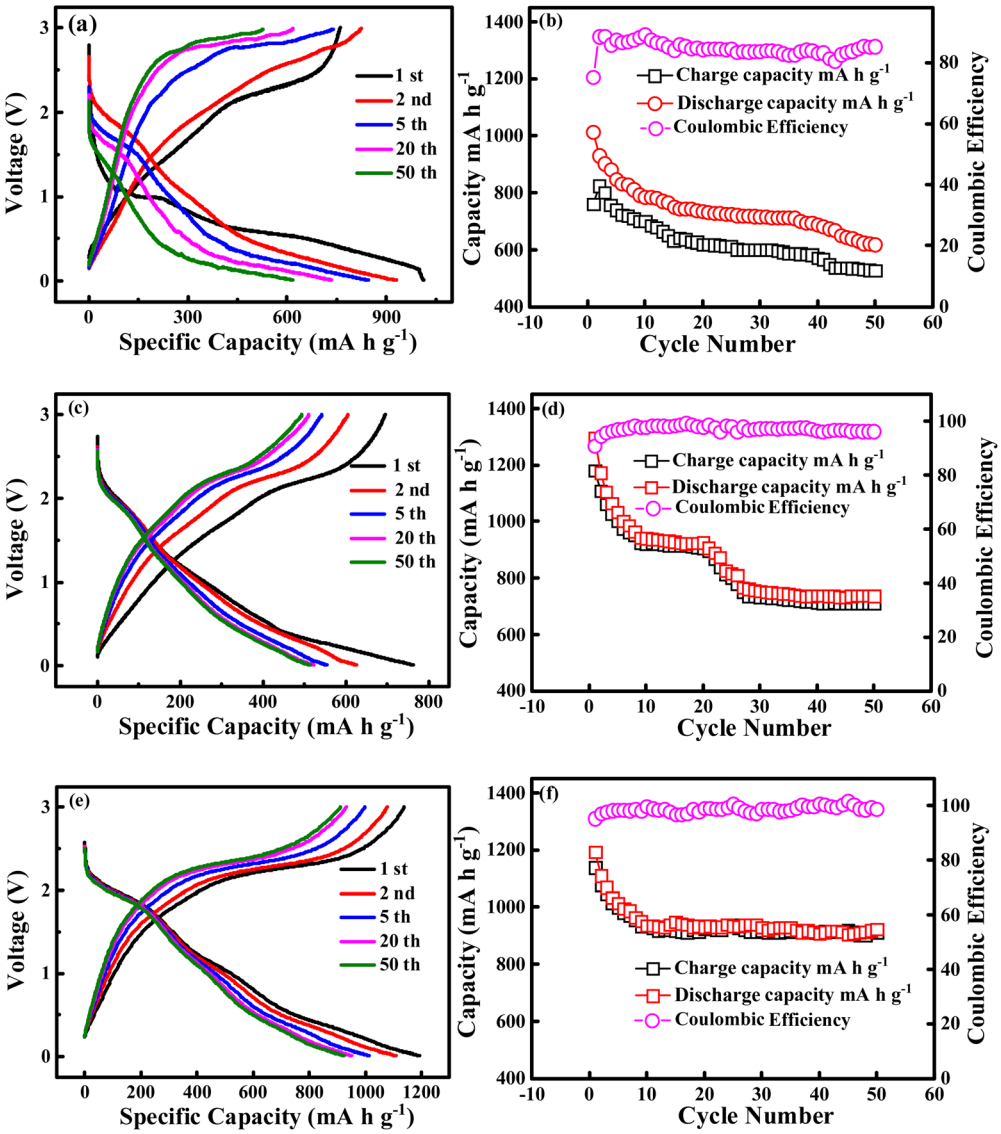

Fig. 5 (a, c and e) Charge–discharge curves, (b, d and f) cycle performance and coulombic efficiency at a current density of 100 mA h g^{-1} for meso-MoS_2–MoP/G (700 °C), meso-MoS_2–MoP/G (750 °C), and meso-MoS_2–MoP/G (800 °C) .

Mo atoms ($0 < \delta \leq 4$). This indicated that $P^{\delta-}$ could induce a charge transfer from Mo to P. The XPS results showed that the existence of the Mo–P bond induced fast electron transfer in MoS_2, leading to strong coupling between MoS_2 and MoP.

To confirm this result, electrochemical behaviors of the meso-MoS_2–MoP/G (700 °C), meso-MoS_2–MoP/G (750 °C), and meso-MoS_2–MoP/G (800 °C) hybrids were investigated using cyclic voltammetry (CV), galvanostatic charging–discharging tests, and electrochemical impedance spectroscopy (EIS).

Fig. 5a, c, and 5e show the charge–discharge curves for meso-MoS_2–MoP/G (700 °C), meso-MoS_2–MoP/G (750 °C), and meso-MoS_2–MoP/G (800 °C) hybrids, obtained at a current density of 100 mA g^{-1}. The meso-MoS_2–MoP/G (700 °C) electrode delivered initial charge and discharge capacities of 829.3 and 687.6 mA h g^{-1}, respectively, with an initial coulombic efficiency of 82.9%. The initial discharge capacities of meso-MoS_2–MoP/G (750 °C) and meso-MoS_2–MoP/G (800 °C) electrode materials were 766.4 and 1192.8 mA h g^{-1}, respectively, and their initial coulombic efficiencies were 90.8% and 95.4%, respectively. The irreversible process in the first cycle led to capacity loss owing to the trapping of Li^+ in the MoS_2 or MoP lattice and the formation of a solid electrolyte interface (SEI). The cycling performances at a current density of 100 mA g^{-1} for these samples are shown in Fig. 5b, d, and f. Clearly, the cycling performance of the meso-MoS_2–MoP/G (800 °C) electrode material was superior to those of meso-MoS_2–MoP/G (700 °C) and meso-MoS_2–MoP/G (750 °C). The 50th discharge capacities of meso-MoS_2–MoP/G (700 °C), meso-MoS_2–MoP/G (750 °C), and meso-MoS_2–MoP/G (800 °C) were 619.6, 514.0, and 910.3 mA h g^{-1}, respectively.

In addition, the rate performances of the samples were evaluated, as shown in Fig. 6a. The meso-MoS_2–MoP/G (800 °C) electrode material exhibited final discharge capacities of 928.5, 839.9, 788.7, and 729.5 mA h g^{-1} at current densities of 100, 200, 500, and 1000 mA g^{-1}, respectively. When the current density returned to 0.1C, the capacity of the meso-MoS_2–MoP/G (800 °C) electrode material recovered to 863.9 mA h g^{-1}, demonstrating good rate capability over a wide range of current densities.

Cyclic voltammetry (CV) was also performed in the voltage range of 0.01 to 3 V at room temperature to investigate the electrochemical behavior. Fig. 6c shows the CV curves of the meso-MoS_2–MoP/G (800 °C) electrode material during the initial three cycles. In the first cycle, the CV curves exhibited two oxidation peaks at 1.50 and 2.27 V, and two corresponding reduction peaks at 0.41 and 1.78 V. In the second cycle, the reduction peak at 1.50 V shifted to a higher potential of 1.60 V. Meantime, compared with the first cycle, the intensity of the reduction peak at 2.27 V decreased, while the oxidation peaks slightly increased. This phenomenon was consistent with the charge–discharge curves shown in Fig. 5e and f.

To better understand the enhanced electrochemical performance of the meso-MoS_2–MoP/G (700 °C), meso-MoS_2–MoP/G (750 °C), and meso-meso-MoS_2–MoP/G (800 °C) electrode materials, electrochemical impedance spectroscopy (EIS) was conducted before cycling, in the frequency range of 10 kHz to 100 MHz. As shown in Fig. 6b, the Nyquist plots of meso-MoS_2–MoP/G (700 °C), meso-MoS_2–MoP/G (750 °C), and meso-MoS_2–MoP/G (800 °C) displayed a semicircle in the high-frequency region and a slope in the low-frequency region. These features

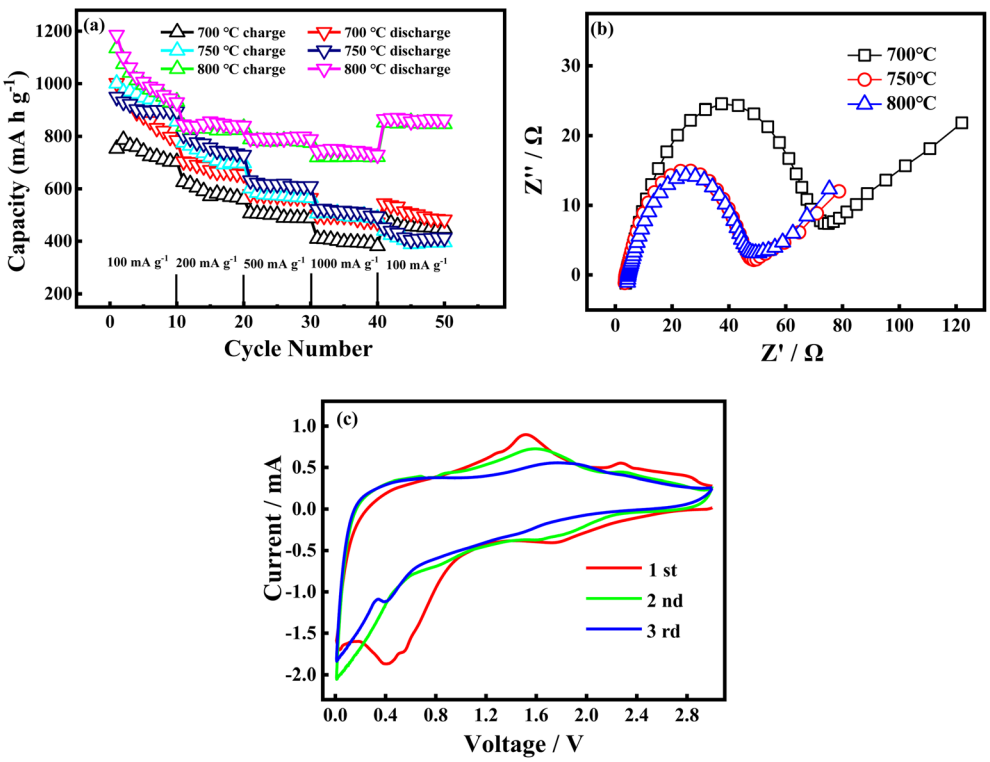

Fig. 6 (a) Rate performance, (b) electrochemical impedance spectra of meso-MoS_2–MoP/G (700 °C), meso-MoS_2–MoP/G (750 °C), and meso-MoS_2–MoP/G (800 °C) hybrids, (c) cyclic voltammetry curves of meso-MoS_2–MoP/G (800 °C) .

were associated with the charge-transfer resistance (R_{ct}) at the electrode–electrolyte interface and the Warburg-type resistance resulting from ion diffusion in the electrode. The resistance values for the meso-MoS_2–MoP/G (750 °C) and meso-MoS_2–MoP/G (800 °C) electrodes were lower than that of meso-MoS_2–MoP/G (700 °C), indicating that the presence of Mo–P bonds in meso-MoS_2–MoP/G (800 °C) significantly reduced charge-transfer resistance. As mentioned in the XPS analysis above, meso-MoS_2–MoP/G (800 °C) possessed Mo–P bond, which induced a charge transfer from molybdenum to phosphorus, thereby downshifting the d-band center of molybdenum in MoP and reducing the Mo–H binding energy. The incorporation of P activated the MoS_2 basal plane, enhancing its activity.[38] This mechanism improved electroconductivity and enhanced the lithium storage properties of the molybdenum-based material.

Combining with the above experimental results, it was inferred that the present Mo–P bond played a vital role in promoting the electrochemical performance. Therefore, pure meso-MoS_2/G without the Mo–P bond was synthesized as a reference sample. Meso-MoS_2/G hybrids were prepared at different temperatures under an Ar/H_2 atmosphere, and the detailed synthesis process is provided in the ESI.† Fig. S1† displays the XRD patterns of meso-MoS_2/G electrode materials obtained at 400 °C, 450 °C, and 500 °C. It can be seen from the XRD patterns that when the calcination temperature reaches 500 °C, all diffraction peaks can be assigned to MoS_2 (JCPDS#74-0932), indicating the successful fabrication of the meso-MoS_2/G (500 °C) hybrid.

The morphology and microstructure of the as-synthesized meso-MoS_2/G hybrids were characterized by SEM. Fig. S2† illustrates the SEM images of meso-MoS_2/G hybrids annealed at 400 °C, 450 °C, and 500 °C for 4 h under a nitrogen atmosphere, where the layered structure and draped morphology of graphene can be clearly observed. Meanwhile, the morphology of the hybrids obtained at different calcination temperatures showed no significant change.

The overall XPS spectra (Fig. S3a†) revealed the presence of Mo, S, and C elements. The C 1s spectrum was deconvoluted into three peaks at 284.7 eV for C–C, 286.1 eV for C–O, and 288.7 eV for O–C=O (Fig. S3b†). Fig. S3c† shows the high-resolution spectrum of Mo, which can be mainly deconvoluted into four peaks. Two intense peaks at 229.3 and 232.5 eV were attributed to the binding energies of Mo $3d_{5/2}$ and Mo $3d_{3/2}$ of Mo^{4+}, respectively. The peak located at 226.5 eV corresponded to S 2s. In addition, the XPS peak at 236.0 eV suggested the presence of MoO_3 species. As shown in Fig. S3d,† the S 2s peaks at approximately 163.3 and 162.2 eV corresponded to the binding energies of S $2p_{1/2}$ and S $2p_{3/2}$, respectively, and the high-energy component at 168.7 eV was assigned to S^{4+} species in sulfate groups (SO_3^{2-}).

Fig. S4† presents the galvanostatic charge–discharge profiles and cycle performance of meso-MoS_2/G (400 °C), meso-MoS_2/G (450 °C), and meso-MoS_2/G (500 °C) hybrids recorded over different cycles at a current density of 100 mA g^{-1}. Their discharge capacities during the first cycle are 937.2, 1122.9, and 796.6 mA h g^{-1}, respectively. After several cycles, the discharge capacities stabilized at 424.1, 508.3, and 526.3 mA h g^{-1}, respectively. Among them, the meso-MoS_2/G (500 °C) hybrid exhibited the highest cycle performance after 50 cycles, but it was still not comparable to meso-MoS_2–MoP/G (800 °C), further confirming the importance of the Mo–P bond in meso-MoS_2–MoP/G.

3. Conclusion

In this paper, two-dimensional (2D) mesoporous ultrasmall MoS_2–MoP heterostructured nanosheets/graphene hybrids (meso-MoS_2–MoP/G) were synthesized using a "nanocasting" method followed by a phosphidation treatment. The as-prepared meso-MoS_2–MoP/G hybrids possessed unique mesoporous structures, with ultrasmall heterostructured MoS_2–MoP nanosheets vertically growing on graphene nanosheets. Furthermore, the Mo–P bond also improved the properties of the molybdenum metal. Benefiting from its unique structure and composition, especially the MoS_2–MoP heterostructure, the 2D meso-MoS_2–MoP/G hybrid demonstrated excellent lithium storage performance as an anode material for lithium-ion batteries, in terms of specific capacity, cycling stability, and long-cycle life. The specific capacity of the meso-MoS_2–MoP/G (800 °C) electrode material remained above 910.3 mA h g^{-1} at a current density of 100 mA g^{-1} after 50 cycles. Even at a high current density of 1 A g^{-1}, the meso-MoS_2–MoP/G (800 °C) hybrid still delivered a remarkable discharge capacity of 863.9 mA h g^{-1} with good cycling stability.

Data availability

The data supporting this article have been included as part of the ESI.†

Conflicts of interest

There are no conflicts to declare.

Acknowledgements

This study was funded by the Innovation and Entrepreneurship Training Program for College Students in 2023 (202310135004); the Innovation and Entrepreneurship Training Program for College Students in 2024 (202410135007); and Basic research funding for 2025 (32150025113, 32150025115).

References

1 L. Zhang, X. Li, M. Yang and W. Chen, High-safety separators for lithium-ion batteries and sodium-ion batteries: advances and perspective, *Energy Storage Mater.*, 2021, **41**, 522–545.
2 C. Yu, S. Huang, H. Xu, J. Yan, K. Rong and M. Sun, Optimal charging of lithium-ion batteries based on lithium precipitation suppression, *J. Energy Storage*, 2024, **82**, 110580.
3 Y. An, Y. Tian, C. Wei, Y. Tao, B. Xi, S. Xiong, J. Feng and Y. Qian, Dealloying: an effective method for scalable

fabrication of 0D, 1D, 2D, 3D materials and its application in energy storage, *Nano Today*, 2021, **37**, 101094.

4 M. Marinaro and S. Dsoke, Advances in Nanomaterials for Lithium-Ion/Post-Lithium-Ion Batteries and Supercapacitors, *Nanomaterials*, 2022, **12**, 2512.

5 R. Sharma, H. Kumar, G. Kumar, S. Sharma, R. Aneja, A. K. Sharma, R. Kumar and P. Kumar, Progress and challenges in electrochemical energy storage devices: Fabrication, electrode material, and economic aspects, *Chem. Eng. J.*, 2023, **468**, 143706.

6 H. Niu, N. Zhang, Y. Lu, Z. Zhang, M. Li, J. Liu, N. Zhang, W. Song, Y. Zhao and Z. Miao, Strategies toward the development of high-energy-density lithium batteries, *J. Energy Storage*, 2024, **88**, 111666.

7 J. Li, J. Fleetwood, W. B. Hawley and W. Kays, From Materials to Cell: State-of-the-Art and Prospective Technologies for Lithium-Ion Battery Electrode Processing, *Chem. Rev.*, 2022, **122**, 903–956.

8 H. Chen, W. Wang, L. Yang, L. Dong, D. Wang, X. Xu, D. Wang, J. Huang, M. Lv and H. Wang, A Review of Cobalt-Containing Nanomaterials, Carbon Nanomaterials and Their Composites in Preparation Methods and Application, *Nanomaterials*, 2022, **12**, 2042.

9 S. Xu, J. V. D. Watt, D. Laudal, R. Zhang, R. Ahmed and X. Hou, Coal-derived carbon anodes for lithium-ion batteries: Development, challenges, and prospects, *J. Power Sources*, 2025, **628**, 235858.

10 R. Naraprawatphong, C. Chokradjaroen, S. Thiangtham, L. Yang and N. Saito, Nanoscale advanced carbons as an anode for lithium-ion battery, *Mat. Today Adv.*, 2022, **16**, 100290.

11 W. Zhong, X. Huang, Y. Lin, Y. Cao and Z. Wang, Compact Co_3O_4/Co in-situ nanocomposites prepared by pulsed laser sintering as anode materials for lithium-ion batteries, *J. Energy Chem.*, 2021, **58**, 386–390.

12 H. Liu, S. Wang, J. Zhao, B. Zhang, L. Liu, R. Bao and Z. Jing, Sn-based anode materials for lithium-ion batteries: From mechanism to modification, *J. Energy Storage*, 2024, **80**, 109862.

13 Y. Zhang, L. Liu, L. Zhao, C. Hou, M. Huang, H. Algadi, D. Li, Q. Xia, J. Wang, Z. Zhou, X. Han, Y. Long, Y. Li, Z. Zhang and Y. Liu, Sandwich-like $CoMoP_2$/MoP heterostructures coupling N, P co-doped carbon nanosheets as advanced anodes for high-performance lithium-ion batteries, *Adv. Compos. Hybrid Mat.*, 2022, **5**, 2601.

14 X. Ding, J. Miao, Y. Yang, L. Liu, Y. Xiao and L. Han, A novel embedded KVO_3/NC anode for high-performance lithium-ion batteries, *J. Colloid Interface Sci.*, 2024, **676**, 755.

15 R. S. A. Saravanan, K. S. Bejigo and S.-J. Kim, Scope and significance of transition metal oxide nanomaterials for next-generation Li-ion batteries, *Mater. Chem. Front.*, 2023, **7**, 4613.

16 W. Ma, X. Zhang, Y. Meng and J. Zhao, Hierarchical carbon/MoS_2 composites as anodes for advanced electrochemical performance, *Ionics*, 2022, **28**, 5499.

17 Q. Ruan, Y. Qian, M. Xue, L. Chen and Q. Zhang, Emerging two-dimensional Mo-based materials for rechargeable metal-ion batteries: Advances and perspectives, *J. Energy Chem.*, 2024, **89**, 487.

18 X. Hu, W. Zhang, X. Liu, Y. Mei and Y. Huang, Nanostructured Mo-based electrode materials for electrochemical energy storage, *Chem. Soc. Rev.*, 2015, **44**, 2376.

19 X. Li, R. Wang, Q. Wu, Y. Yu, T. Gao, T. Yao, X. Wang, J. Han and B. Song, Synergistically Designed Dual Interfaces to Enhance the Electrochemical Performance of MoO_2/MoS_2 in Na- and Li-Ion Batteries, *Small*, 2023, **19**, 2206940.

20 R. Liu, H. Zeng, Y. Peng, Y. Wang and F. Ran, A pinning structure *via* composing laminar rGO with fragmented MoS_2 toward fast and stable sodium and lithium-ion storage, *J. Alloys Compd.*, 2023, **968**, 172028.

21 X. Liu, P. Mei, Y. Dou, R. Luo, Y. Yamauchi and Y. Yang, Heteroarchitecturing a novel three-dimensional hierarchical MoO_2/MoS_2/carbon electrode material for high-energy and long-life lithium storage, *J. Mater. Chem. A*, 2021, **9**, 13001.

22 J. Ru, T. He, B. Chen, Y. Feng, L. Zu, Z. Wang, Qi. Zhang, T. Hao, R. Meng, R. Che, C. Zhang and J. Yang, Covalent Assembly of MoS_2 Nanosheets with SnS Nanodots as Linkages for Lithium/Sodium-Ion Batteries, *Angew. Chem., Int. Ed.*, 2020, **59**, 14621.

23 F. Zeng, H. Liu, Y. Pan, M. Yu, Y. Qu and C. Yuan, Encapsulating N-Doped Carbon Nanorod Bundles/MoO_2 Nanoparticles *via* Surface Growth of Ultrathin MoS_2 Nanosheets for Ultrafast and Ultralong Cycling Sodium Storage, *ACS Appl. Mater. Interfaces*, 2020, **12**, 6205.

24 X. Liu, P. Mei, Y. Dou, R. Luo, Y. Yamauchi and Y. Yan, Heteroarchitecturing a novel three-dimensional hierarchical MoO_2/MoS_2/carbon electrode material for high-energy and long-life lithium storage, *J. Mater. Chem. A*, 2021, **9**, 13001.

25 M. Cai, H. Zhang, Y. Zhang, B. Xiao, L. Wang, M. Li, Y. Wu, B. Sa, H. Liao, L. Zhang, S. Chen, D.-L. Peng, M.-S. Wang and Q. Zhang, Boosting the potassium-ion storage performance enabled by engineering of hierarchical MoSSe nanosheets modified with carbon on porous carbon sphere, *Sci. Bull.*, 2022, **67**, 933.

26 T. Li, S. Gao, K. Li, G. Liu, X. Sheng, D. Shang, L. Wu, S. Chen, Y. Wang and S. Wu, Tailoring the phase evolution of molybdenum-based nanocrystals in carbon nanofibers for enhanced performance of lithium-ion batteries, *J. Alloys Compd.*, 2023, **934**, 168042.

27 H. Lu, K. Tian, L. Bu, X. Huang, X. Li, Y. Zhao, F. Wang, J. Bai, L. Gao and J. Zhao, Synergistic effect from coaxially integrated CNTs@MoS_2/MoO_2 composite enables fast and stable lithium storage, *J. Energy Chem.*, 2021, **55**, 449.

28 Z. Yan, Z. Huang, H. Zhou, X. Yang, S. Li, W. Zhang, F. Wang and Y. Kuang, Facile fabrication of MoP nanodots embedded in porous carbon as excellent anode material for potassium-ion batteries, *J. Energy Chem.*, 2021, **54**, 571.

29 Y. Wang, D. Zhang, Y. Yanga, Y. Guo, Z. Bai, P. K. Chuc and Y. Luo, Three-dimensional nano/micro-structured porous MoP/CNTs microspheres as high-capacity anode for lithium-ion batteries, *J. Alloys Compd.*, 2021, **872**, 159608.

30 Y. Shen, Y. Jiang, Z. Yang, J. Dong, W. Yang, Q. An and L. Mai, Electronic structure modulation in MoO_2/MoP heterostructure to induce fast electronic/ionic diffusion kinetics for lithium storage, *Adv. Sci.*, 2022, **9**, 2104504.

31 X. Wang, N. Deng, J. Ju, G. Wang, L. Wei, H. Gao, B. Cheng and W. Kang, Flower-like heterostructured MoP–MoS_2 hierarchical nanoreactor enabling effective anchoring for LiPS and enhanced kinetics for high performance Li-S batteries, *J. Membrane Sci.*, 2022, **642**, 120003.

32 D. Li, G. Lin, Z. Huang, X. Tang, Z. Wu, Z. Li, D. Zhang, P. Chuangchanh and R. Zeng, Effect of different shell structure on lithium storage properties of MoS_2 anode, *Electroanal. Chem.*, 2022, **905**, 115972.

33 Z. Lin, Z. Wu, Y. Wu, H. Jia, X. Hu, M. Yu and X. H. S. Ying, Synthesis of polyhedral MoS_2@C hollow cages using a sacrificial template approach for improved reversible lithium storage, *Phys. Chem. Chem. Phys.*, 2025, **27**, 8167–8173.

34 S. Guo, Y. Zhang, S. Tang, B. Wang, Y. Wang, Y. Song, X. Xin, Y. Zhang and X. Lia, Tuning interlayer spacing of MoS_2 for enhanced hydrogen evolution reaction, *J. Alloys Compd.*, 2021, **864**, 158581.

35 H. Ma, W. Yan, Y. Yu, L. Deng, Z. Hong, L. Song and L. Li, Phosphorus vacancies improve the hydrogen evolution of MoP electrocatalysts, *Nanoscale*, 2023, **15**, 1357.

36 Q. Zhou, J. Feng, X. Peng, L. Zhong and R. Sun, Porous carbon coupled with an interlaced MoP–MoS_2 heterojunction hybrid for efficient hydrogen evolution reaction, *J. Energy Chem.*, 2020, **45**, 45–51.

37 C. Deng, F. Ding, X. Li, Y. Guo, W. Ni, H. Yan, K. Suna and Y.-M. Yan, Templated-preparation of a three-dimensional molybdenum phosphide sponge as a high performance electrode for hydrogen evolution, *J. Mater. Chem. A*, 2016, **4**, 59.

38 R. Ye, P. del Angel-Vicente, Y. Liu, M. J. Arellano-Jimenez, Z. Peng, T. Wang, Y. Li, B. I. Yakobson, S. H. Wei, M. J. Yacaman and J. M. Tour, High-Performance Hydrogen Evolution from $MoS_{2(1-x)}P_x$ Solid Solution, *Adv. Mater.*, 2016, **28**, 1427–1432.